ELSEVIER

J. Non-Newtonian Fluid Mech. 146 (2007) 30–44

Journal of Non-Newtonian Fluid Mechanics

www.elsevier.com/locate/jnnfm

A two-dimensional numerical study of the stick–slip extrusion instability

Eleni Taliadorou [a,1], Georgios C. Georgiou [a,*], Andreas N. Alexandrou [b,2]

[a] *Department of Mathematics and Statistics, University of Cyprus, P.O. Box 20537, 1678 Nicosia, Cyprus*
[b] *Department of Mechanical and Manufacturing Engineering, University of Cyprus, P.O. Box 20537, 1678 Nicosia, Cyprus*

Received 14 June 2006; received in revised form 17 November 2006; accepted 21 November 2006

Abstract

The time-dependent, compressible extrusion of a Carreau fluid is solved over the reservoir-die-extrudate region using finite elements in space and a fully implicit scheme in time. A nonmonotonic slip law based on experimental data on polyethylene melts is assumed to hold along the die wall and the velocity at the entrance of the reservoir is taken to be fixed and uniform. As in the case of the extrudate-swell flow, the combination of compressibility and nonlinear slip leads to self-sustained oscillations of the pressure drop and of the mass flow rate in the unstable regime. The effects of the reservoir volume, the imposed flow rate, and the capillary length on the amplitude and the frequency of the pressure and free surface oscillations are studied and comparisons are made with experimental observations.

Keywords: Stick–slip instability; Extrudate-swell flow; Carreau model; Compressibility; Slip

1. Introduction

Among the various types of polymer extrusion instabilities, the stick–slip instability is the only one that is associated with pressure oscillations at constant throughput, i.e. at constant piston speed in the reservoir region [1]. The instantaneous flow rate at the capillary exit is also oscillatory and the extrudate emerges from the capillary in bursts, and is characterized by alternating rough and relatively smooth zones. It is well known that the pressure and flow rate oscillations follow the stable branches of the apparent flow curve, i.e. the plot of the wall shear stress, σ_w, versus the apparent shear rate, γ_A, as shown in Fig. 1. The apparent wall shear rate is calculated from the volumetric flow rate Q as follows

$$\dot{\gamma}_A \equiv \frac{32Q}{\pi D^3}, \tag{1}$$

where D is the diameter of the capillary. The wall shear stress is calculated by

$$\sigma_w = \frac{P_d - P_{end}}{4L/D}, \tag{2}$$

where P_d is the driving pressure determined for the force on the piston, P_{end} the Bagley end correction for the pressure drop, and L is the length of the capillary.

Due to the oscillations of the wall shear stress, the flow curve is discontinuous and consists of two stable positive-slope branches separated by the unstable stick–slip instability regime [2–5], as illustrated in Fig. 1. Experiments with fluids exhibiting the stick–slip instability revealed that the flow curve depends on the capillary diameter. This dependence, which becomes stronger as the apparent shear rate increases, is due to the occurrence of slip at the capillary wall. The lower part of the low-flow rate branch is insensitive to the capillary diameter, which implies the absence of wall slip. The upper part may be weakly dependent on D, which indicates that weak slip is possible [6–8]. The high-flow rate branch is strongly dependent on D, which is an indication of strong slip [6–11]. Based on slip velocity estimates, Hatzikiriakos and Dealy [2] proposed a power-law slip equation for the right branch of their flow curve. El Kissi and Piau [10] also derived a single nonmonotonic slip equation for both the

* Corresponding author. Tel.: +357 22892612; fax: +357 22892601.
E-mail addresses: georgios@ucy.ac.cy (G.C. Georgiou), andalexa@ucy.ac.cy (A.N. Alexandrou).
[1] Tel.: +357 22892612; fax: +357 22892601.
[2] Tel.: +357 22892256.

0377-0257/$ – see front matter © 2006 Elsevier B.V. All rights reserved.
doi:10.1016/j.jnnfm.2006.11.005

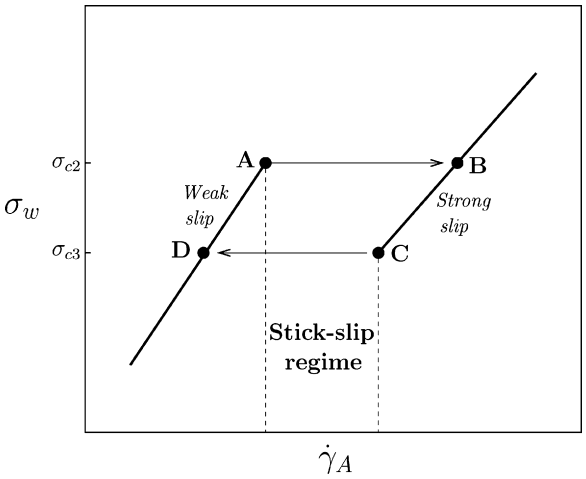

Fig. 1. Schematic of an apparent flow curve and the stick–slip regime.

branches of the flow curve. These indirect observations for the occurrence of stick and slip phenomena during the extrusion of certain polymer melts have also been confirmed by recent direct slip velocity measurements with optical methods [12,13]. The role of wall slip in extrusion instabilities is discussed in detail in [14,15].

When the imposed shear rate is in the unstable regime, the wall shear stress and the apparent shear rate oscillate (with the same period and phase) following closely, in the clockwise sense, the hysteresis cycle ABCD [2,3,5]. The critical wall shear stresses for the nearly instantaneous jumps from point A to point B and from C to D are denoted here by σ_{c2} and σ_{c3}, respectively. These two critical stresses correspond to the transition from weak to strong slip and vice versa, and define the limiting values between which the wall shear stress oscillates. Hence, the amplitude of the wall shear stress oscillation is equal to $(\sigma_{c2} - \sigma_{c3})$. Similarly, the amplitudes of the sudden apparent shear rate increase and decrease are determined by the shear rate differences between points A and B and points C and D, respectively [2,3]. Hence, for a given capillary (i.e. given D and L/D), the onset of the stick–slip instability (i.e. the critical shear stress σ_{c2}) and the amplitudes of the oscillations are determined solely by the steady-state flow curve [2,3,16,17].

The oscillations of the pressure and the extrudate flow rate are obviously analogous to those of the wall shear stress and apparent flow rate, respectively. The variation of the extrudate flow rate, in spite of the constant piston speed, arises from the compressibility of the melt in the reservoir, and causes the characteristic appearance of the extrudate which consists of alternating rough and relatively smooth regions [2–4].

The generation of self-sustained pressure and flow rate oscillations when compressibility is combined with nonlinear slip has been confirmed by the two-dimensional simulations of Georgiou and Crochet [18,19]. These authors employed an arbitrary nonmonotonic slip equation relating the wall shear stress to the slip velocity and numerically solved the time-dependent compressible Newtonian Poiseuille and extrudate-swell flows. Their simulations showed that steady-state solutions in the negative-slope regime of the flow curve are unstable, and that oscillatory solutions are obtained at constant volumetric flow rate. In a recent work, Georgiou [20] carried out numerical simulations for a shear-thinning Carreau fluid using an empirical slip equation that is based on the experimental measurements of Hatzikiriakos and Dealy with a HDPE melt [2,8]. His time-dependent calculations at fixed volumetric flow rates in the unstable negative-slope regime of the flow curve showed that the pressure and flow rate oscillations do not follow the stable branches of the flow curve, in contrast to the experiments. As stated in Ref. [20], including the reservoir region in the simulations is necessary in order not only to account for the compression and decompression of most part of the fluid but also for obtaining limit cycles following the steady-state branches of the flow curve, i.e. for getting pressure and extrudate flow rate oscillations characterized by abrupt changes, as is the experiments.

The objective of the present work is to extend the simulations in [20] to the full reservoir-capillary-extrudate geometry, in order (a) to study the effects of the reservoir length, the imposed flow rate, and the capillary length on the pressure and free surface oscillations and (b) to make comparisons with experimental observations on extrusion under constant piston speed. As discussed below, experimental results from different studies are not always in agreement. The present simulations may be helpful in understanding some of the experimental observations.

Experiments with different materials showed that as the reservoir is emptying, the period of the pressure and flow rate oscillations is reduced while the hysteresis loop of the flow curve remains unchanged, which implies that the amplitudes of the pressure and flow rate oscillations remain the same [2,3,7,16,17,21]. The period of the oscillations has been found to vary linearly with the volume of the melt in the reservoir, and that the extrapolations of the experimental period data do not pass through the origin [2,3,5,22,23]. On the other hand, the waveform of the pressure oscillations appears to be insensitive to the reservoir length, meaning that the relative durations of the compression and relaxation phases do not change as the extrusion experiment proceeds [2,3,17].

According to experimental observations, as the imposed flow rate is increased in the unstable regime, the waveform of the pressure oscillations changes so that the relative duration of the compression part is reduced, while their amplitude is not affected [2,3,17,21,24]. The reports concerning the effect on the period of the pressure and flow rate oscillations are somehow conflicting. In experiments with HDPEs, Hatzikiriakos and Dealy [2], Durand et al. [3] and Den Doelder et al. [25] observed that the period is decreased as the flow rate is increased. A period reduction has also been reported in experiments on a LLDPE [7] and a PB [26]. On the other hand, the earlier experiments of Myerholtz [21], Weill [17] and Okubo and Hori [27] on HDPEs and those of Vinogradov et al. [24] on PBs showed that the period passes through a minimum in the unstable regime.

Experiments with HDPEs have shown that as the capillary length increases, the stick–slip regime is shifted to lower volumetric flow rates and its size increases, the hysteresis loop of the flow curve becomes larger, and both the amplitude and the period

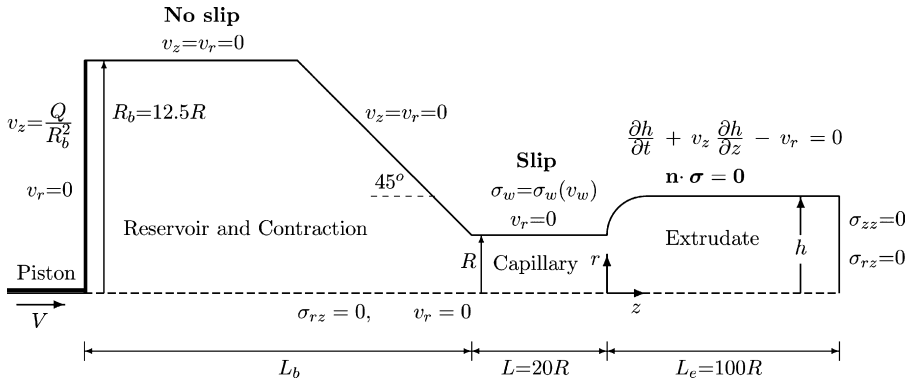

Fig. 2. Geometry and boundary conditions for the time-dependent, compressible, axisymmetric extrusion of a Carreau fluid with slip along the capillary wall, including the reservoir region.

of the pressure oscillations increase [2,3,5]. The experiments of Durand et al. [3] and Vergnes et al. [28] showed that reducing the capillary length eventually leads to a continuous (monotonic) flow curve. According to Den Doelder et al. [25], HDPEs do not exhibit pressure oscillations for short dies ($L/D<5$), since these are overruled by the entry and exit pressure losses.

The critical wall shear stress, σ_{c2}, at which the stick–slip instability is observed may increase or decrease or remain constant as the capillary length to the capillary diameter ratio, L/D, increases. Experiments with HDPE melts [2,3,5,21] and EPDM compounds [28] showed that σ_{c2} and the stress difference $(\sigma_{c2}-\sigma_{c3})$ increase with the capillary length. Hatzikiriakos and Dealy [2] attribute this effect to the pressure dependence of wall slip. Experiments with other materials, however, show that σ_{c2} is not always an increasing function of the L/D ratio. This was found to slightly decrease with L/D in the experiments of Vinogradov et al. with PBs [24], El Kissi and Piau with PDMS [9], and Kalika and Denn with a LLDPE [7], and to be independent of L/D in the experiments of Ramamurthy with a LLDPE [6] and Wang and Drda with entangled linear PEs [29,30].

In Section 2, the governing equations, the slip equation, and the boundary and initial conditions are presented and their dimensionless forms are provided. In Section 3, after a brief description of the numerical method, the numerical results are presented and discussed and comparisons are made with experimental observations. Finally, Section 4 summarizes the conclusions.

2. Governing equations

The geometry of the flow corresponds to the actual setup used in the experiments of Hatzikiriakos and Dealy [2]. There is a contraction region at 45° between the barrel and the capillary as shown in Fig. 2. The actual values of the radii of the barrel and the capillary, denoted respectively by R_b and R, and the length of the capillary, L, are tabulated in Table 1.

The continuity and the momentum equations for time-dependent, compressible, isothermal viscous flow in the absence of body forces are as follows

$$\frac{\partial \rho}{\partial t} + \nabla \cdot \rho \mathbf{v} = 0, \tag{3}$$

$$\rho\left(\frac{\partial \mathbf{v}}{\partial t} + \mathbf{v}\cdot\nabla\mathbf{v}\right) = \nabla\cdot\boldsymbol{\sigma}, \tag{4}$$

where ρ is the density, $\mathbf{v}$ the velocity vector, p the pressure, and $\boldsymbol{\sigma}$ is the stress tensor. For the density, the following linear equation is employed:

$$\rho = \rho_0[1+\beta(p-p_0)], \tag{5}$$

where β is the isothermal compressibility and ρ_0 is the density at the reference pressure p_0.

Even though the fluid studied by Hatzikiriakos and Dealy [2] is considered to behave as a power-law one, we employ the Carreau model in order to avoid the well-known numerical difficulties caused by the former model, which predicts infinite zero-shear-rate viscosity. For compressible flow of a Carreau fluid with zero infinite-shear-rate viscosity, the stress tensor is written as

$$\boldsymbol{\sigma} = -p\mathbf{I} + \eta_0[1+\lambda^2(2\mathrm{II}_\mathbf{d})^2]^{(n-1)/2}\left(2\mathbf{d} - \frac{2}{3}\mathbf{I}\nabla\cdot\mathbf{v}\right), \tag{6}$$

where $\mathbf{I}$ is the unit tensor, $\mathbf{d}$ is the rate-of-deformation tensor, defined as

$$\mathbf{d} = \frac{1}{2}[(\nabla\mathbf{v}) + (\nabla\mathbf{v})^{\mathrm{T}}], \tag{7}$$

the superscript T denotes the transpose, $\mathrm{II}_\mathbf{d}$ the second invariant of $\mathbf{d}$, η_0 the zero-shear-rate viscosity, λ a time constant, and n is the power-law exponent.

Table 1
Symbols and values of various lengths concerning the flow geometry

Symbol	Parameter	Value
R_b	Radius of the barrel	0.9525 cm
L_b	Length of the barrel	
	Contraction angle	45°
R	Capillary radius	3.81×10^{-2} cm
L	Capillary length	0.762 cm
L_e	Length of the extrudate	3.81 cm

Table 2
Values of the slip model parameters

Parameter	Value
a_1 ((MPa)$^{-m_1}$ cm/s)	125.09
m_1	3.23
a_2 ((MPa)$^{-m_2}$ cm/s)	1000
m_2	2.86
a_3 ((MPa)$^{-m_3}$ cm/s)	5.484×10^{-3}
m_3	−4.434
σ_{c2} (MPa)	0.27
σ_{min} (MPa)	0.19
v_{c2} (cm/s)	1.82
v_{min} (cm/s)	8.65

2.1. The slip equation

We use the same three-branch multi-valued slip model as in [20]:

$$v_w = \begin{cases} a_1\sigma_w^{m_1}, & 0 \le v_w \le v_{c2} \\ a_3\sigma_w^{m_3}, & v_{c2} \le v_w \le v_{min} \\ a_2\sigma_w^{m_2}, & v_w \le v_{min} \end{cases}, \tag{8}$$

where v_w is the relative velocity of the fluid with respect to the wall, σ_w the shear stress on the wall, v_{c2} the maximum slip velocity at σ_{c2}, and v_{min} is the minimum slip velocity at σ_{min}. The values of all slip parameters are given in Table 2. The plot of the slip equation is given in Fig. 3. This is based on the experimental data of Hatzikiriakos and Dealy [8]. The low-flow rate (low velocity) branch is a simplification of the corresponding slip equation proposed by the latter authors, under the assumption of infinite normal stress. The high-flow rate branch is exactly the power-law slip equation proposed by the same authors for the right branch of their experimental flow curve. The intermediate branch, which corresponds to the unstable region of the flow curve, is just an arbitrary line connecting the other two branches. It should be noted that for a finite normal stress the first branch of the slip equation moves closer to the third one; for zero normal stress, the two branches almost overlap. It should be noted that in reality, the wall shear stress is expressed as a function of the slip velocity and not vice versa, i.e. $\sigma_w = \sigma_w(v_w)$. In other words, the inverse of Eq. (8) is used.

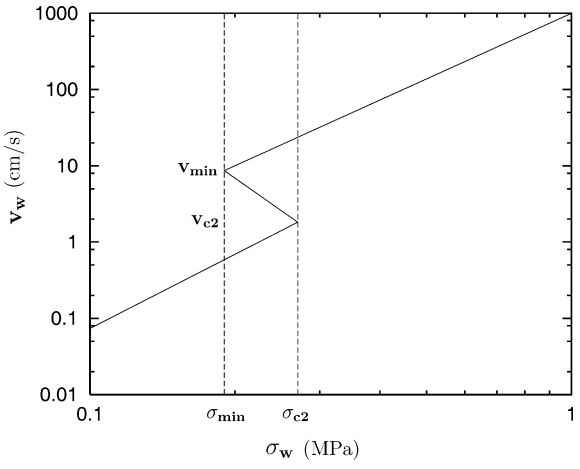

Fig. 3. The nonmonotonic slip law based on the experimental data of Hatzikiriakos and Dealy [2,8].

2.2. Dedimensionalization

To dedimensionalize the governing equations, we scale the lengths by the capillary radius R, the velocity by a reference velocity, V, in the capillary, the pressure and the stress components by $\eta_0\lambda^{n-1}V^n/R^n$, the density by ρ_0, and the time by R/V. With these scalings, one gets:

$$\frac{\partial\rho}{\partial t} + \nabla\cdot\rho\mathbf{v} = 0, \tag{9}$$

$$Re(1+Bp)\left(\frac{\partial\mathbf{v}}{\partial t} + \mathbf{v}\cdot\nabla\mathbf{v}\right) = \nabla\cdot\boldsymbol{\sigma}, \tag{10}$$

and

$$\boldsymbol{\sigma} = -p\mathbf{I} + \Lambda^{1-n}[1+\Lambda^2(2\mathrm{II}_\mathbf{d})^2]^{(n-1)/2}\left(2\mathbf{d} - \frac{2}{3}\mathbf{I}\nabla\cdot\mathbf{v}\right), \tag{11}$$

where all variables are now dimensionless. (For simplicity the same symbols are used for the dimensionless variables.) The dedimensionalization results in three dimensionless numbers, the Reynolds number, Re, the compressibility number, B, and Λ in the constitutive equation, which are defined as follows

$$Re \equiv \frac{\rho_0 R^n V^{2-n}\lambda^{1-n}}{\eta_0}, \qquad B \equiv \frac{\beta\eta_0 V^n}{\lambda^{1-n}R^n}, \qquad \Lambda \equiv \frac{\lambda V}{R}. \tag{12}$$

For resin A at 180 °C, Hatzikiriakos and Dealy [2] provide the following values: $\beta = 9.923 \times 10^{-4}$ MPa^{-1}, $n = 0.44$ and, for the consistency index, $K = 0.0178$ MPa s^n. Assuming that $\eta_0 = 0.03$ MPa s, we calculate λ from $\eta_0\lambda^{n-1} = K$. For the reference velocity, we get $V = R\dot{\gamma}/4 = 5.24$ cm/s^2, assuming that $\dot{\gamma} = 500$ s^{-1} and $R = 3.81 \times 10^{-2}$ cm^2. Under these assumptions, the values of the three dimensionless numbers are: $Re = 1.43 \times 10^{-5}$, $B = 1.54 \times 10^{-4}$, and $\Lambda = 349.2$.

The dimensionless form of the slip equation is

$$v_w = \begin{cases} A_1\sigma_w^{m_1}, & 0 \le v_w \le v_{c2} \\ A_3\sigma_w^{m_3}, & v_{c2} \le v_w \le v_{min} \\ A_2\sigma_w^{m_2}, & v_w \le v_{min} \end{cases}, \tag{13}$$

where

$$A_i \equiv \frac{a_i\eta_0^{m_i}V^{m_i n-1}}{\lambda^{m_i(1-n)}R^{m_i n}}, \quad i = 1, 2, 3, \tag{14}$$

and the dimensionless values of v_{c2} and v_{min} correspond to

$$\sigma_{c2}^* \equiv \frac{\sigma_{c2}R^n\lambda^{1-n}}{\eta_0 V^n} \quad \text{and} \quad \sigma_{min}^* \equiv \frac{\sigma_{min}R^n\lambda^{1-n}}{\eta_0 V^n}, \tag{15}$$

respectively. The values of the above dimensionless numbers are given in [20].

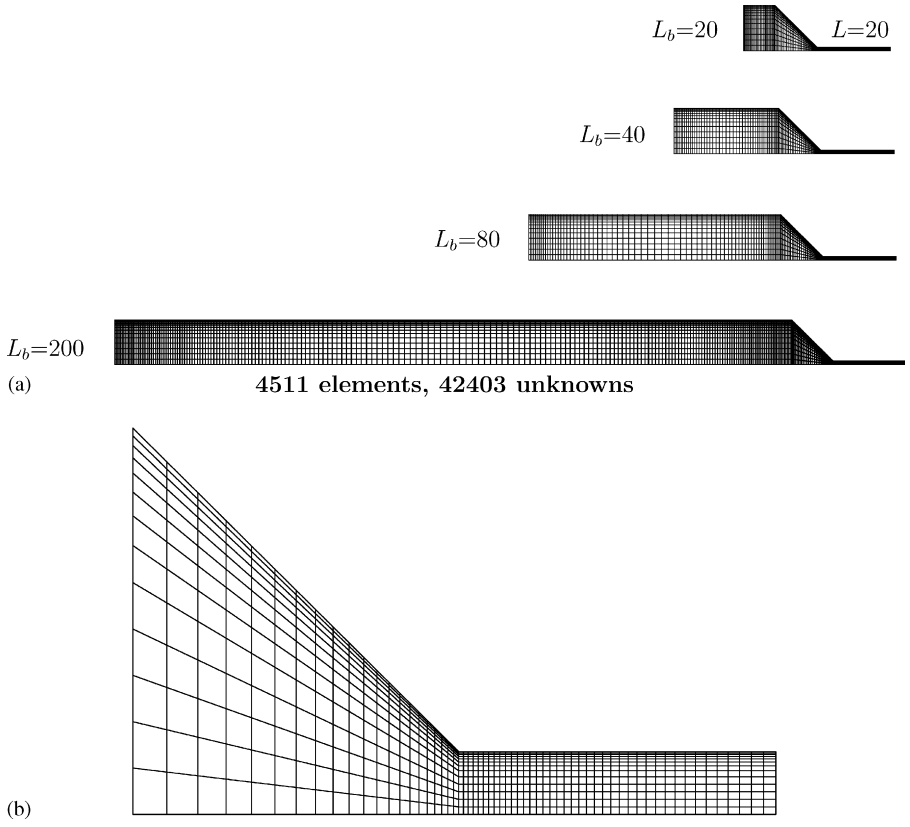

Fig. 4. (a) Various meshes for different barrel lengths and $L = 20$ used in the simulations (the extrudate region is excluded). (b) Detail of the meshes near the die entrance.

2.3. Boundary and initial conditions

The dimensionless boundary conditions for the full extrusion flow are shown in Fig. 2. The usual symmetry conditions apply along the axis of symmetry. Along the barrel and the contraction walls both velocity components are zero (no slip). Along the capillary wall, only the radial velocity is zero, whereas the axial velocity satisfies the slip Eq. (13). At the inlet plane, it is assumed that the radial velocity component is zero while the axial velocity is uniform (corresponding to the motion of the piston at constant speed):

$$v_z = \frac{Q}{R_b^2},$$

where Q is the imposed volumetric flow rate (scaled by $\pi R^2 V$). It should be noted that the simulations are carried out on a fixed domain, i.e. the motion of the piston is not taken into account. This is a reasonable assumption provided that the piston speed is low.

When the extrudate region is excluded, we assume that the radial velocity component vanishes at the capillary exit. In the case of the extrudate-swell flow, the weaker condition $\sigma_{rz} = 0$ is used at the outflow plane. In both cases, the total normal stress is assumed to be zero, $\sigma_{zz} = 0$. Finally, on the free surface, we assume that surface tension is zero and impose vanishing normal and tangential stresses. Additionally, the unknown position $h(z, t)$ of the free surface satisfies the kinematic condition:

$$\frac{\partial h}{\partial t} + v_z \frac{\partial h}{\partial z} - v_r = 0. \tag{16}$$

When the extrudate region is excluded, we use as initial condition the steady-state solution corresponding to a given volumetric flow rate Q_{old} at the inlet that we perturb to Q at $t = 0$. In the case of the extrudate-swell flow, we start with the steady-state solution of the stick–slip flow (i.e. with flat free surface) for a given volumetric flow rate Q and release the free surface at $t = 0$.

3. Numerical results

The finite element formulation is used for solving the free surface flow problem under study. The unknown position of the free surface is calculated simultaneously with the velocity and pressure fields (full-Newton method). The standard biquadratic-velocity (P^2-C^0) and bilinear-pressure (P^1-C^0) elements with a quadratic representation for the position h of the free surface are employed. For the spatial discretization, the standard Galerkin forms of the continuity, momentum and kinematic equations are used, while for the time discretization, the standard fully implicit (Euler backward-difference) scheme has been chosen.

As already mentioned, the dimensionless capillary length is $L = 20$. In order to study the effect of the capillary length on the stick–slip instability, additional capillary lengths are considered

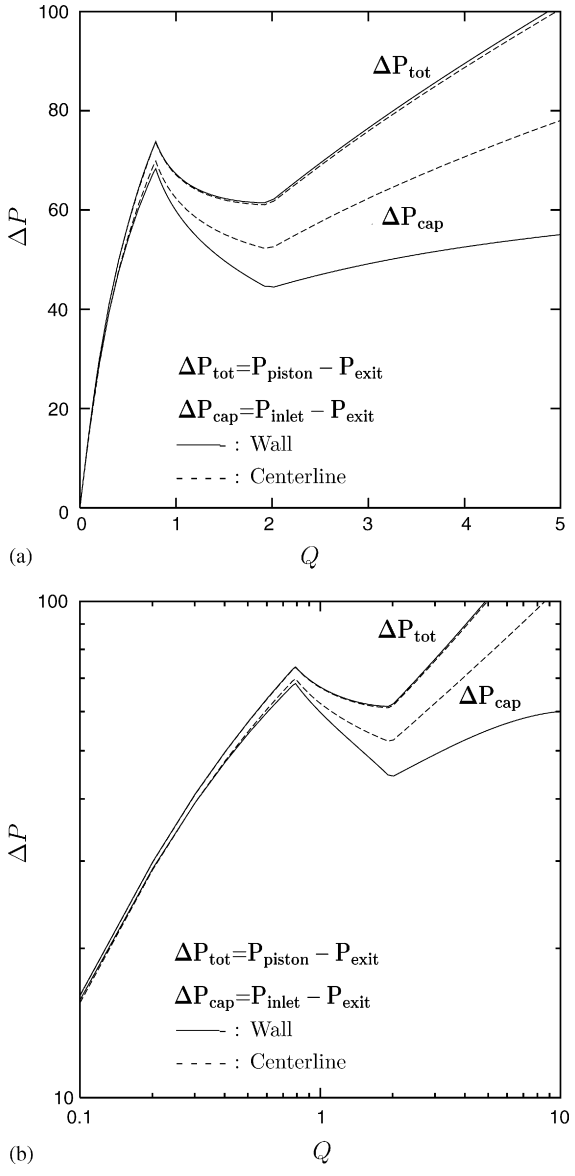

Fig. 5. Newtonian flow curves with $Re = 0.01$ and $L_b = 80$: (a) regular plot; (b) log–log plot.

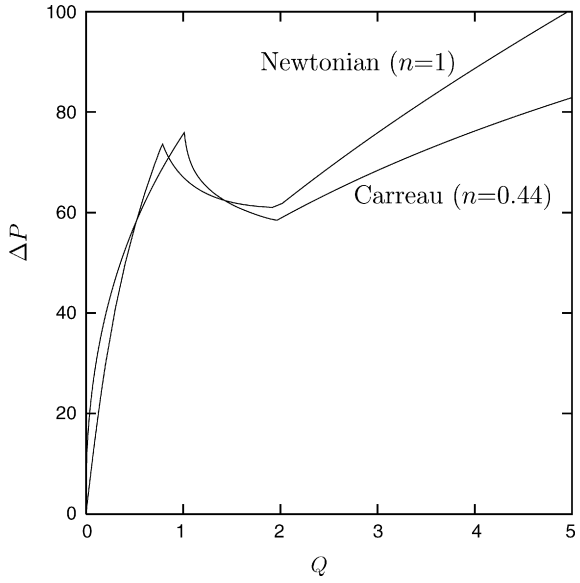

Fig. 6. Effect of the power-law exponent on the flow curve: $Re = 0.01$ and $L_b = 80$.

in the last part of this section. The extrudate length L_e has been taken to be 100, while the reservoir length L_b ranged from 20 to 200. Fig. 4 shows some of the meshes used in the simulations (excluding the extrudate region) with $L = 20$. The finite element meshes were refined near the walls, and around the entrance and exit of the capillary. The longest mesh ($L_b = 200$) consisted of 4511 elements in the reservoir-capillary region and of 18,386 elements when the extrudate region was included. The corresponding total numbers of unknowns were 42,403 and 169,504, respectively. With the exception of the Reynolds number, Re, the values of the dimensionless parameters are those given in Section 2, i.e. $B = 1.54 \times 10^{-4}$ and $\Lambda = 349.2$. For comparison purposes, in addition to the Carreau flow ones ($n = 0.44$), results are also presented for the Newtonian flow ($n = 1$).

We first constructed the steady-state flow curves for the reservoir-capillary region (excluding the extrudate region). In Fig. 5, we show both the regular (Fig. 5a) and log–log (Fig. 5b) plots of the pressure drop versus the volumetric flow rate obtained with $Re = 0.01$ and $L_b = 80$ in the case of Newtonian flow. Four different possibilities for the pressure drop are shown: (a) $\Delta P_{tot,w}$ is the pressure difference along the wall from the piston to the capillary exit; (b) $\Delta P_{tot,c}$ is the pressure difference along the centerline from the piston to the capillary exit; (c) $\Delta P_{cap,w}$ is the pressure difference along the wall from the capillary entrance to the capillary exit; (d) $\Delta P_{cap,c}$ is the pressure difference along the centerline from the capillary entrance to the capillary exit. The pressures $\Delta P_{tot,w}$ and $\Delta P_{tot,c}$ are essentially the same for all volumetric flow rates and correspond to the piston driving pressure, P_d, in Eq. (2). $\Delta P_{cap,w}$ and $\Delta P_{cap,c}$ are slightly different from $\Delta P_{tot,w}$ and $\Delta P_{tot,c}$ along the left positive-slope branch of the flow curve. Much bigger differences are observed in the negative-slope and the right positive-slope branches of the flow curves. In these regimes, $\Delta P_{cap,w}$ is much lower than $\Delta P_{cap,c}$ due to the effect of the singularity at the capillary entrance. It should be noted that differences between $\Delta P_{tot,w}$ and $\Delta P_{tot,c}$ at high volumetric flow rates are much bigger in the case of the Carreau fluid. A careful examination of the solution near the piston region shows that these differences are solely due to the region near the piston and the barrel wall. Moreover, unlike their Newtonian counterparts, $\Delta P_{cap,w}$ and $\Delta P_{cap,c}$ almost coincide, which implies that the effect of the singularity at the capillary entrance is much weaker than in the Newtonian case. In what follows, the pressure drop ΔP corresponds to the piston pressure $\Delta P_{tot,c} = P_d$, unless otherwise indicated.

The flow curves obtained in the case of Carreau flow ($n = 0.44$) are quite similar. In Fig. 6, the Newtonian and Carreau flow curves ($\Delta P = \Delta P_{tot,c}$) are compared. We observe that as n is reduced, the negative-slope regime is slightly shifted to the right and reduces in size. Moreover, the resulting hysteresis loop, which is also shifted to the right, is much bigger. This implies that one would expect slightly bigger pressure oscillations and much bigger jumps of the volumetric flow rate. From Fig. 6,

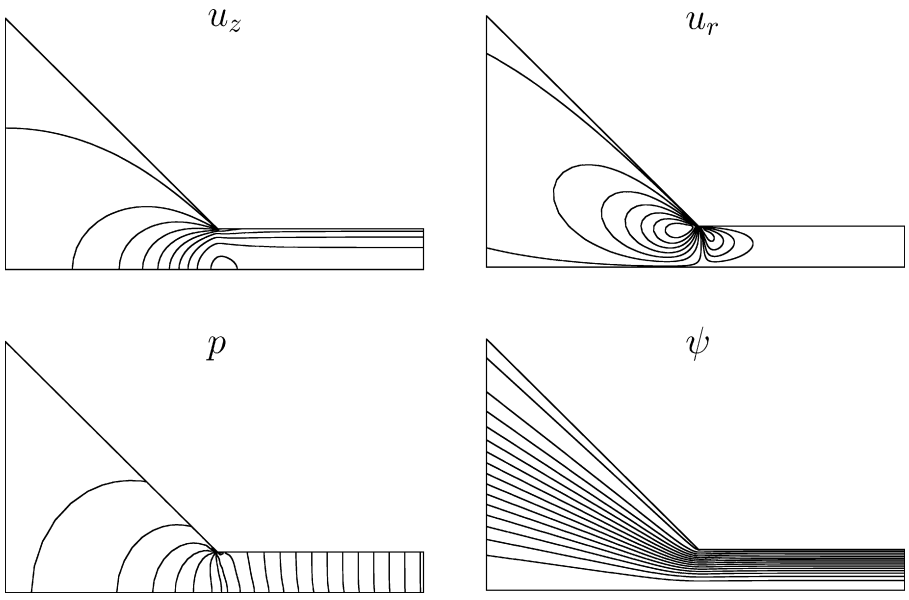

Fig. 7. Contours of the steady-state Carreau solution ($n = 0.44$) inside the barrel and the die (the extrudate-region has been excluded) for $Re = 0.01$, $L_b = 80$ and $Q = 1.5$.

it can be deduced that the biggest volumetric flow rate will be about eight times its lowest value. This agrees well with the report of Hatzikiriakos and Dealy [2] that with resin A at 160 °C the mass flow rate suddenly increases by a factor of about 8.

Fig. 7 shows the (steady-state) contours of the two velocity components, the pressure and the streamfunction, ψ, obtained for the Carreau flow with $Re = 0.01$, $L_b = 80$, and $Q = 1.5$, i.e. near the middle of the negative-slope regime of the flow curve. We see the rearrangement of the flow near the capillary entrance, and observe that the differences between ΔP_{tot} and ΔP_{cap} are basically due to the entrance region. Far from the capillary entrance, the pressure in the reservoir is practically constant, which verifies that one of the basic assumptions made in one-dimensional phenomenological models proposed in the literature (see, e.g. Ref. [31]) is valid.

When the extrudate region is excluded, the steady-state solutions are perturbed by changing the volumetric flow rate from an old value to the desired one, Q. Given that the flow is compressible, the behavior of the time-dependent solution depends on whether the new value of Q corresponds to the stable positive-slope branches or to the unstable negative-slope one. In the former case, the new steady-state is obtained without any oscillations, whereas, in the latter one, the solution is oscillatory and becomes periodic after a transition period. Self-sustained oscillations of the pressure drop and the mass flow rate are obtained which are similar to those observed experimentally in the stick–slip extrusion instability regime. All the results presented below have been obtained in the unstable regime.

In Fig. 8, we show the oscillations of the pressure drop and the volumetric flow rate obtained by perturbing the Newtonian steady-state solution for $Re = 0.01$, $L_b = 80$ and $Q = 1.35$. We note in Fig. 8a that sudden jumps of the pressure drop are observed when this is measured across the capillary. No jumps are observed when ΔP is measured between the piston and the capillary exit. The volumetric flow rate at the capil-

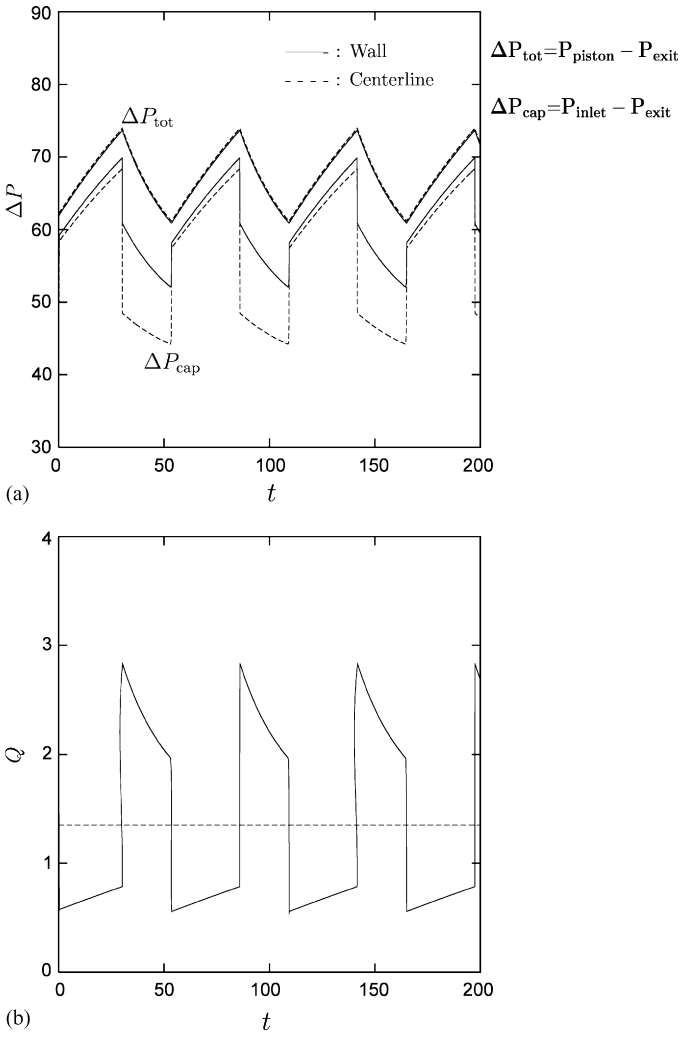

Fig. 8. Pressure and flow rate oscillations for Newtonian flow ($n = 1$), $Re = 0.01$, $L_b = 80$ and $Q = 1.35$.

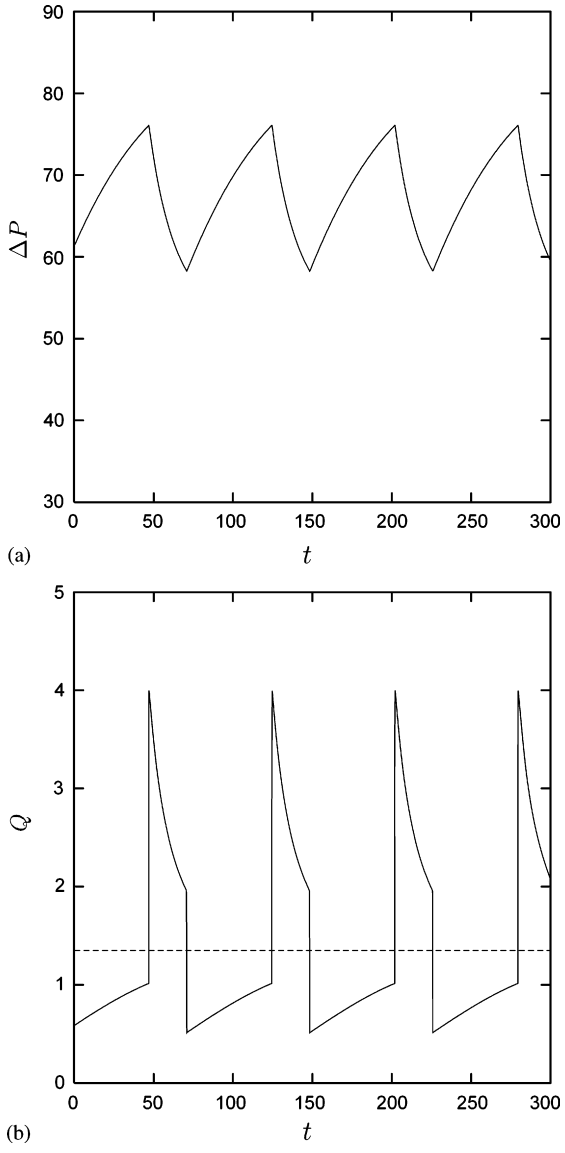

Fig. 9. Pressure and flow rate oscillations for Carreau flow ($n = 0.44$), $Re = 0.01$, $L_b = 80$ and $Q = 1.35$.

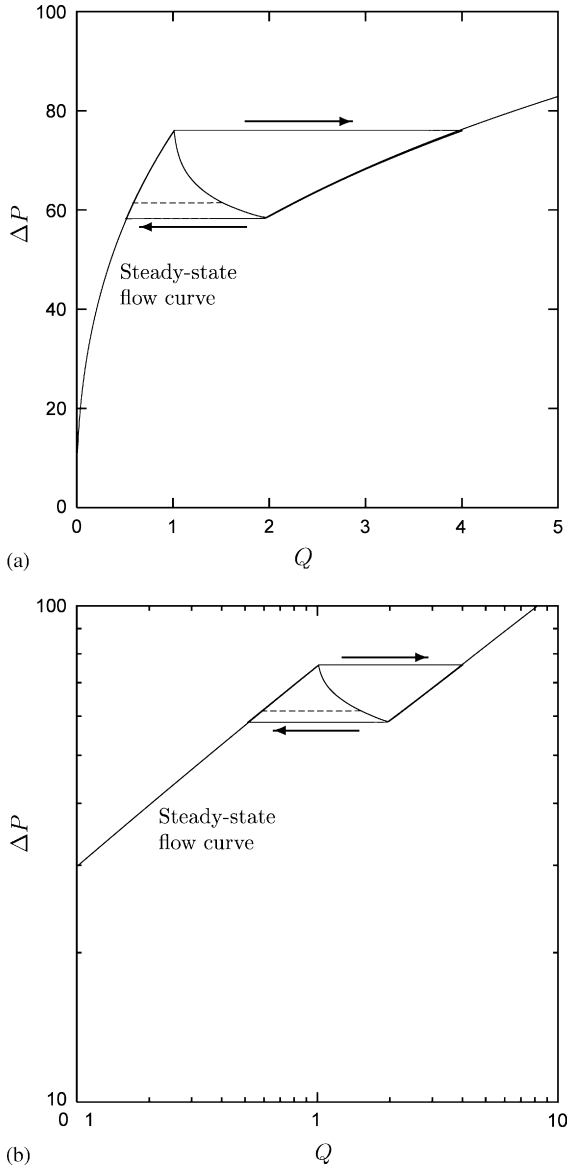

Fig. 10. Trajectory of the solution on the flow curve plane for Carreau flow ($n = 0.44$), $Re = 0.01$, $L_b = 80$ and $Q = 1.35$: (a) regular plot; (b) log–log plot.

lary exit (Fig. 8b) is also characterized by sudden jumps which is consistent with experimental observations [2,3]. The results in the case of Carreau flow are similar but the amplitude and the period of the oscillations are higher (Fig. 9), as expected. Plotting the trajectory of the solution on the flow curve plane (Fig. 10) shows that, after a transition period, a limit cycle is reached which follows exactly the positive-slope branches of the steady-state flow curve. The volumetric flow rate increases together with the pressure following exactly the left positive-slope branch of the flow curve and, when the pressure reaches its maximum value, Q jumps to the right positive-slope branch. The volumetric flow rate then starts decreasing together with the pressure following this branch till the pressure reaches its minimum and then jumps to the left positive-slope branch and starts the next oscillation cycle. This behavior agrees well with experimental observations [2,3]. Note also that in our previous study [20], the limit cycles did not follow the steady-state flow curve due to the omission of the reservoir region. This drawback was also exhibited by the one-dimensional model of Greenberg and Demay [32], which does not include the barrel region. Note that most one-dimensional phenomenological relaxation/oscillation models require as input the experimental (steady-state) flow curve. These models are based on the compressibility/slip mechanism and describe oscillations of the pressure and the volumetric flow rate in the stick–slip instability regime (see [11,31,33] and references therein) under the assumption that these follow the experimental flow curve. The present simulations are the first to predict that the limit cycle indeed follows the steady-state flow curve.

In an attempt to approach the experimental value $Re = 1.43 \times 10^{-5}$, we reduced the value of the Reynolds number from 0.01 to 0.001. Fig. 11 shows a comparison of the pressure and flow rate oscillations during a cycle, obtained with $Re = 0.01$ and 0.001 for both the Newtonian and the Carreau flows (with

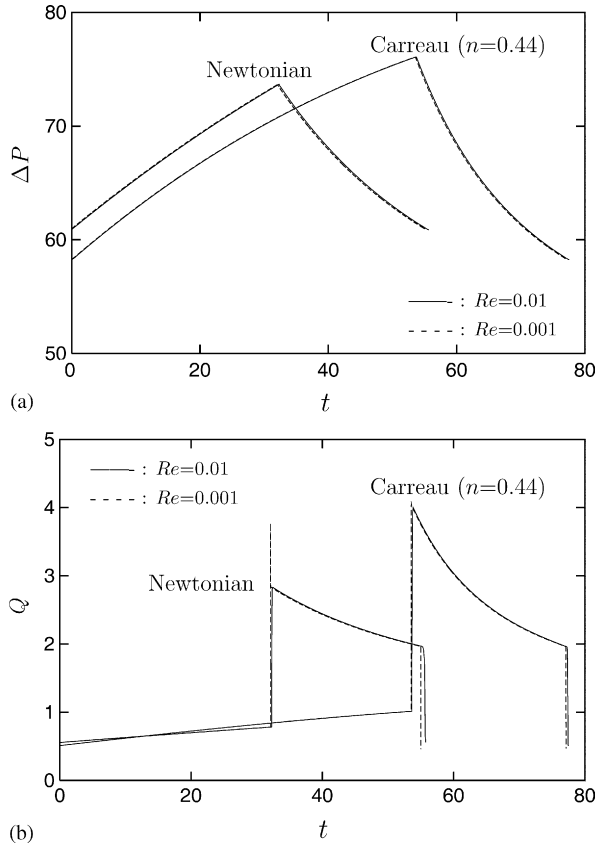

Fig. 11. Comparison of the pressure (a) and flow rate (b) oscillations for $Re = 0.01$ and 0.001, $L_b = 80$ and $Q = 1.35$.

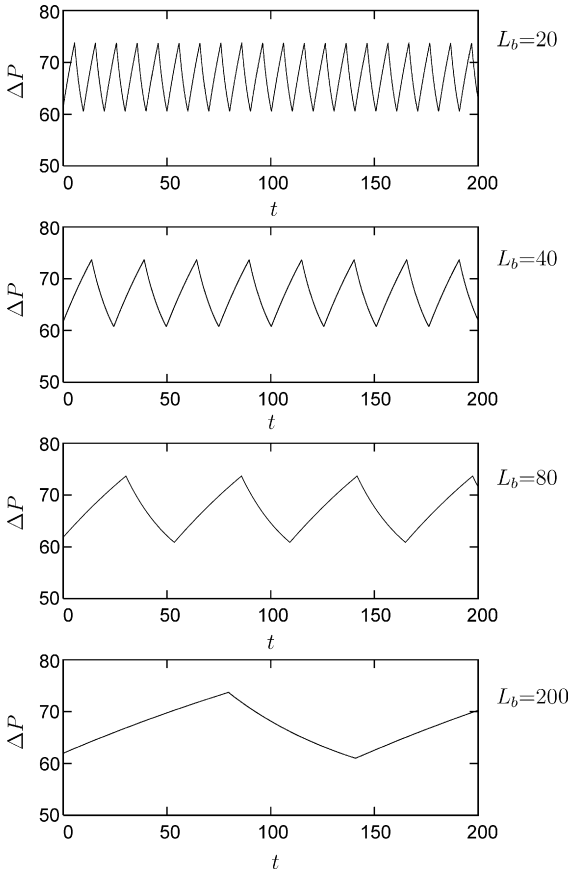

Fig. 12. Effect of the reservoir length on the pressure oscillations: Newtonian flow ($n = 1$), $Re = 0.01$ and $Q = 1.35$.

$L_b = 80$ and $Q = 1.35$). It is clear that decreasing the Reynolds number has no practical effect on the oscillations with the exception of the artificial flow rate overshoots obtained with the lower Re. Instead of trying to eliminate the overshoots by reducing the time step (which would have resulted into much longer runs), we decided to continue the runs with $Re = 0.01$. Note that when the reservoir region is excluded, the results are sensitive to the Reynolds number: the amplitude of the pressure drop oscillations is reduced, the amplitude of the mass flow rate oscillations is increased and the frequency of the oscillations is considerably increased, as the Reynolds number is reduced [20]. This shows once again the importance of including the reservoir region.

In order to study the effect of the reservoir length on the pressure oscillations, we obtained results for various values of L_b. The pressure oscillations for different values of L_b, $Re = 0.01$ and $Q = 1.35$ are given in Figs. 12 and 13 for the Newtonian and the Carreau flow, respectively. In both cases, the period of the pressure oscillations increases with L_b while their amplitude seems to be less sensitive. This is more clearly shown in Fig. 14, where the corresponding periods and the amplitudes of the pressure oscillations are plotted versus the reservoir volume. As already mentioned, the period and the amplitude of the pressure oscillations are higher in the case of the Carreau fluid. In agreement with experiments [2,3,5,23], the period T increases linearly with the reservoir volume, while the amplitude is essentially constant. However, the period appears to pass through the origin, which is not the case with the experiments [2,3,5,23].

To show the effect of the reservoir length on the waveform of the pressure oscillations, we compare in Fig. 15 the normalized pressure oscillations during one cycle for both fluids, $L_b = 20$ and 200. The waveform is independent of the reservoir length, i.e. the durations of both the compression and the relaxation increase linearly with the reservoir length, which agrees well with the experiments of Hatzikiriakos and Dealy [2] and Durand et al. [3].

Results for various values of Q in the unstable regime, $Re = 0.01$ and $L_b = 80$, have been obtained in order to investigate the effect of the imposed volumetric flow rate on the pressure oscillations. Fig. 16 shows the periods of the resulting pressure oscillations versus Q for both the Newtonian and Carreau flows. The period decreases initially reaching a minimum in the middle of the unstable regime and then starts increasing slowly. This was also the case in the experiments of Myerholtz [21], Okubo and Hori [27] and Weill [17] on HDPEs and those of Vinogradov et al. [24] on a polybutadiene. In other experiments, Hatzikiriakos and Dealy [2], Durand et al. [3] and Robert et al. [23] reported that the period decreases with Q. However, the latter authors carried out experiments only for a few values of Q, which were not sufficient for capturing the minimum and the slight increase of the period in the rightmost part of the unstable regime.

The effect of Q on the pressure oscillations is illustrated in Figs. 17 and 18 for the Newtonian and Carreau flows, respectively, where pressure oscillations obtained with $Re = 0.01$,

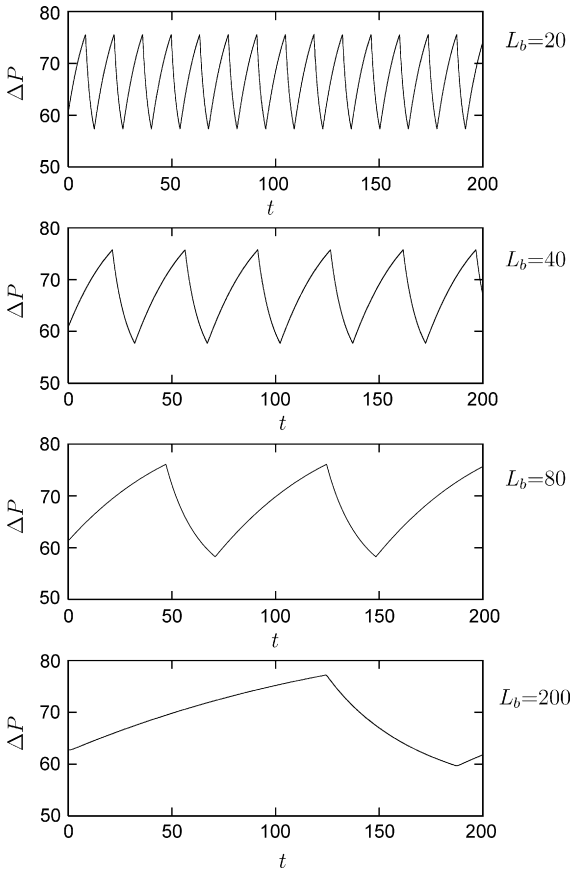

Fig. 13. Effect of the reservoir length on the pressure oscillations: Carreau flow ($n=0.44$), $Re=0.01$ and $Q=1.35$.

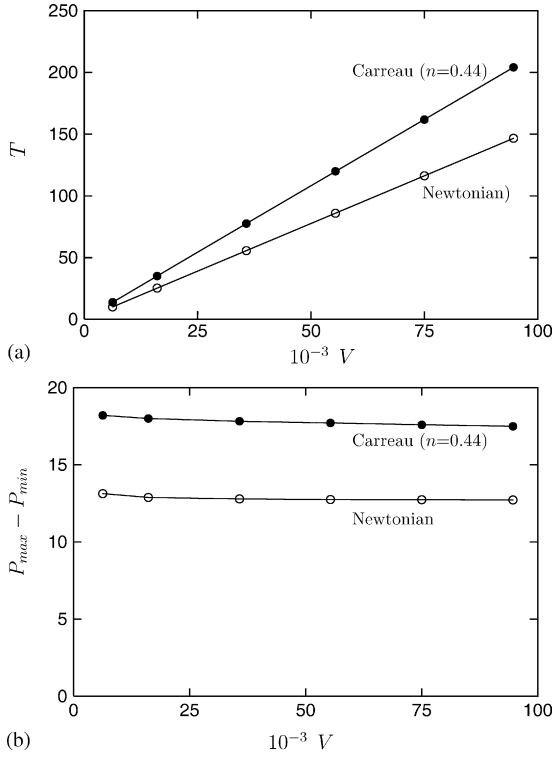

Fig. 14. Period (a) and amplitude (b) of the pressure oscillations vs. the reservoir volume: $Re=0.01$ and $Q=1.35$.

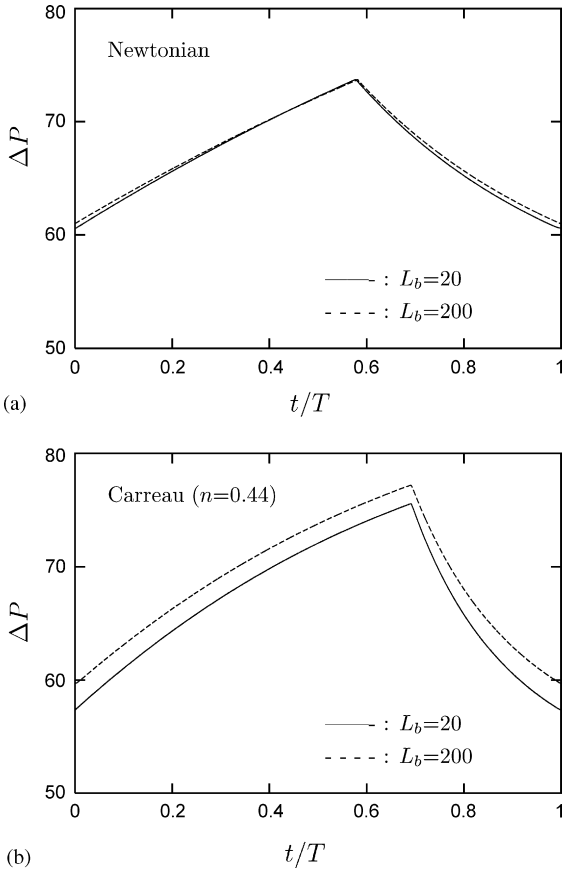

Fig. 15. Effect of the reservoir length on the waveform of the pressure oscillations: (a) Newtonian flow ($n=1$); (b) Carreau flow ($n=0.44$), $Re=0.01$ and $Q=1.35$.

$L_b=80$ and various values of Q are shown. It is again clear that the period of the oscillations passes though a minimum. The ascending part (compression) of the oscillations is relatively reduced in agreement with experimental observations [2,3,23,27]. The descending part of the oscillation does not remain constant but increases significantly at high values of Q, in disagreement with the experiments of Hatzikiriakos and Dealy [2], Durand et al. [3] and Robert et al. [23], in which, however, the period was found to be a decreasing value of Q. In the present simulations, the period is decreasing only in the first half of the unstable regime, where the growth of the descending part of the oscillation is not as pronounced.

The time-dependent simulations of the full extrusion flow have been obtained by starting with the steady-state solution corresponding to a flat free surface (stick–slip flow) and letting the free surface move at $t=0$. In Fig. 19, we present free surface profiles obtained for the Newtonian flow with $Re=0.01$, $Q=1.5$ and a small reservoir length, $L_b=20$, during one cycle of the pressure oscillations (from a pressure drop maximum to the next one) after the periodic solution is established. The free surface oscillations resemble to the 'bamboo' instability pattern with a long 'smooth' part and a shorter 'distorted' part. As in Ref. [20], in addition to the motion of the free surface waves in the flow direction, the free surface also oscillates in the radial direction; swelling is minimized at pressure drop max-

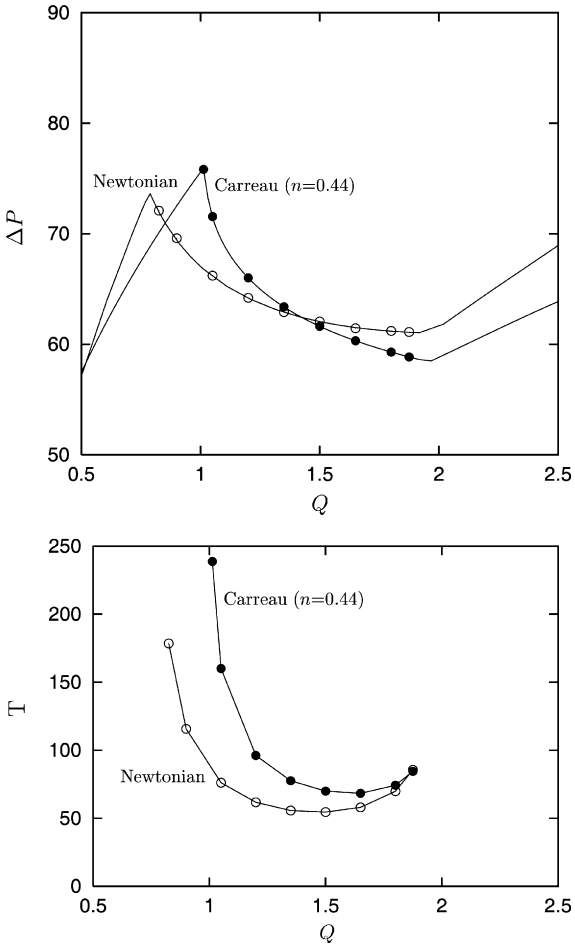

Fig. 16. Effect of the imposed volumetric flow rate on the period of the pressure oscillations: $Re = 0.01$ and $L_b = 80$.

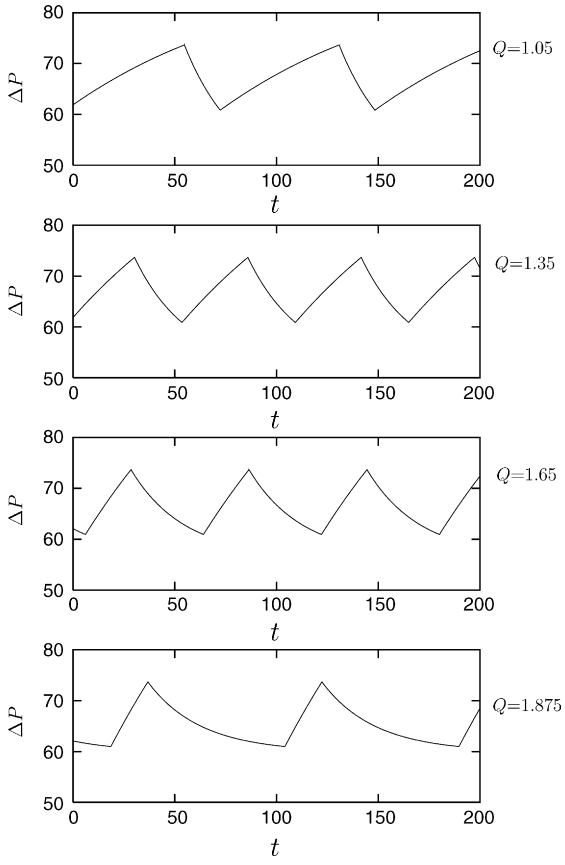

Fig. 17. Effect of the imposed volumetric flow rate on the pressure oscillations: Newtonian flow ($n = 1$), $Re = 0.01$ and $L_b = 80$.

ima. This result agrees with the experiments of Pérez-González et al. [34], who worked with polyethylene melts and observed that severe contractions in the extrudate diameter occur at pressure maxima. From Fig. 19, it can easily be deduced that the motion of the extrudate is accelerated just after the pressure drop maximum, which is, of course, due to the sudden jump of the volumetric flow rate from the left to the right stable branch of the flow curve. Similarly, the extrudate motion is decelerated just after the pressure drop minimum, since the flow rate jumps from the right to the left stable branch. A comparison with Fig. 20, where Newtonian free surface profiles obtained with $L_b = 80$ are shown, reveals that with a longer reservoir (i.e. for a bigger period of pressure oscillations), the wavelength of the resulting free surface waves is much bigger. The amplitude and the relative length of the distortions also appear to increase. Similar results have been obtained for the case of Carreau flow, as illustrated in Figs. 21 and 22, which show free surface profiles obtained with $L_b = 20$ and 80, respectively.

In addition to $L = 20$, we have also considered the values $L = 0.1, 1, 5, 10$ and 40, in order to study the effect of the capillary length. In Fig. 23a, we plotted the flow curves of the Carreau fluid obtained for all capillary lengths. As expected, the pressure drop as well as the difference between its maximum and minimum values are reduced as the capillary length is decreased. Moreover, for very small capillary lengths the flow curve becomes monotonic, which implies that the flow is stable for all values of the volumetric flow rate. In other words, the hysteresis loop decreases in size and eventually vanishes as the capillary length is decreased. As a consequence, the amplitude and the period of the pressure drop oscillations decrease, as illustrated in Fig. 23b; for $L = 1$, no oscillations are observed, since the flow is everywhere stable. Fig. 24 shows that the period and the amplitude of the pressure drop oscillations vary linearly with the capillary length, above the critical value at which the flow curve ceases to be monotonic. These results agree well with experiments on HDPEs [3,5,8,21], regarding the size of the hysteresis loop and the amplitude and the period of the pressure oscillations. Unlike the experiments, however, our simulations do not predict the shift of the stick–slip regime to lower flow rates. This may be due to the fact that the pressure dependence of wall slip is not taken into account in the slip model [2]. The numerical simulations also showed that the capillary length has a slight effect on the waveform of the pressure oscillations. As illustrated in Fig. 25, where the normalized pressure oscillations for $L = 5$, 10 and 40 are compared, the increasing part of the oscillation increases slightly with the capillary length.

Assuming that the pressure drop corresponding to the very short capillary length $L = 0.1$ (see Fig. 23a) is equal to the Bagley end correction, P_{end}, in Eq. (2), we calculated the wall shear stresses versus the apparent wall shear rate. Interestingly, the

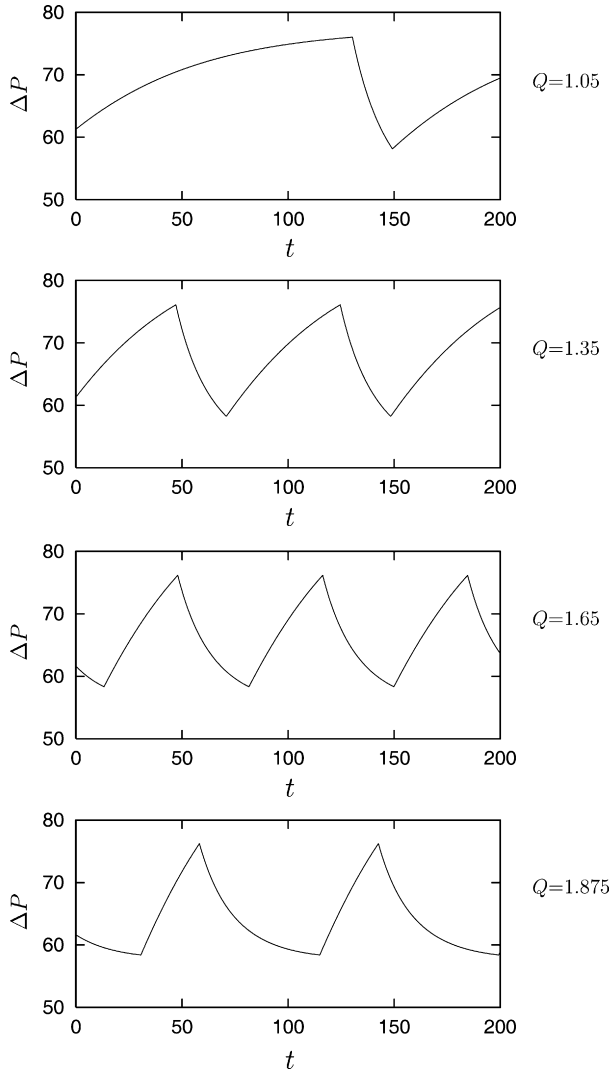

Fig. 18. Effect of the imposed volumetric flow rate on the pressure oscillations: Carreau flow ($n = 0.44$), $Re = 0.01$ and $L_b = 80$.

curves of the calculated wall shear stresses for all capillary lengths ($L = 1$, 5, 10, 20 and 40) coincide, as shown in Fig. 26. The critical values of the wall shear stress are $\sigma_{c2} = 0.34$ MPa and $\sigma_{c3} = 0.24$ MPa, which give $(\sigma_{c2} - \sigma_{c3}) = 0.1$ MPa. The values of σ_{c2} reported by Hatzikiriakos and Dealy [2] are in the range 0.22–0.50 MPa, while those of $(\sigma_{c2} - \sigma_{c3})$ are in the range 0.03–0.11 MPa. Given the assumptions made in the present work, the agreement between simulations and experiments is rather good. As already mentioned, experimental observations on the effect of the capillary length on the value of σ_{c2} cover all possibilities. In some cases, σ_{c2} has been found to increase [2,3,5,28] and in others to decrease [9,7,24], as L is increased. Our simulations agree with the experiments of Ramamurthy [6] and Wang and Drda [29,30] in which σ_{c2} was found to be independent of L. Finally, the effect of the capillary length on the free surface oscillations is illustrated in Fig. 27. Both the amplitude and the wavelength increase, and the waveform appears to change dramatically with the capillary length.

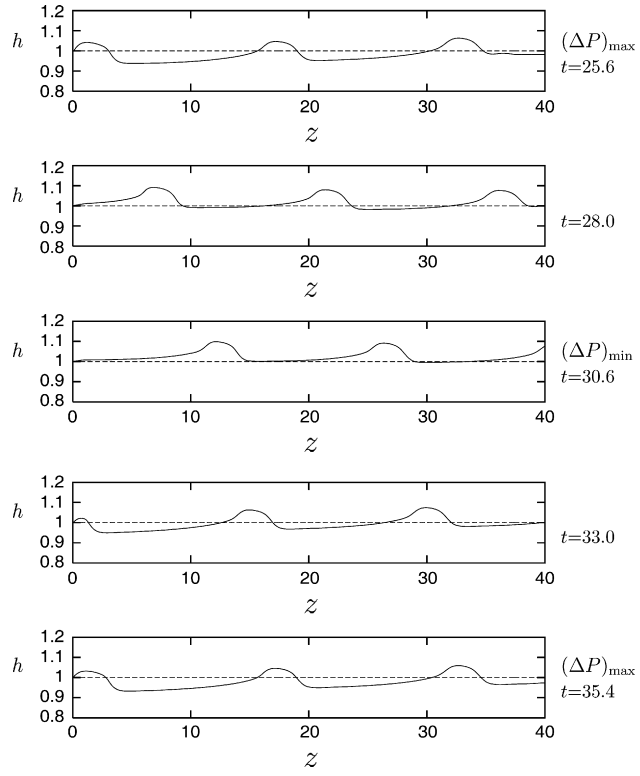

Fig. 19. Free surface oscillations during one cycle: Newtonian flow ($n = 1$), $Re = 0.01$, $L_b = 20$ and $Q = 1.5$.

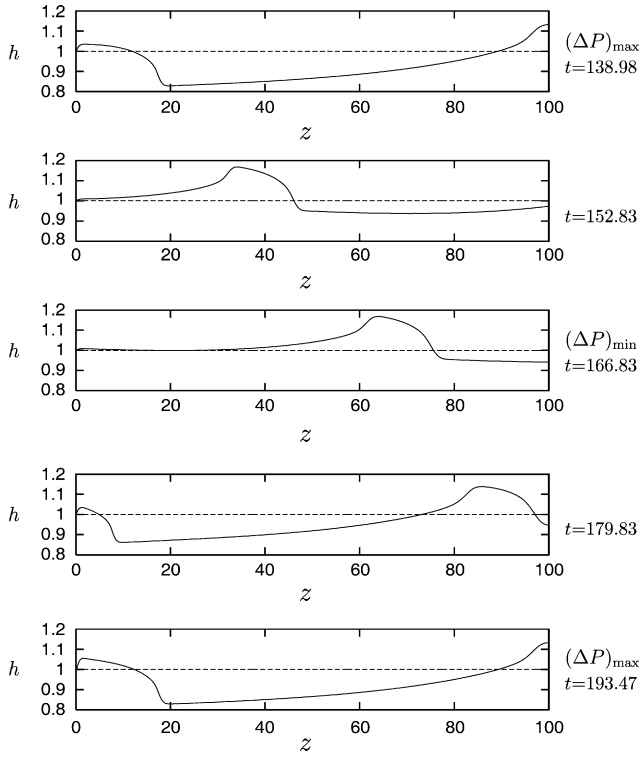

Fig. 20. Free surface oscillations during one cycle: Newtonian flow ($n = 1$), $Re = 0.01$, $L_b = 80$ and $Q = 1.5$.

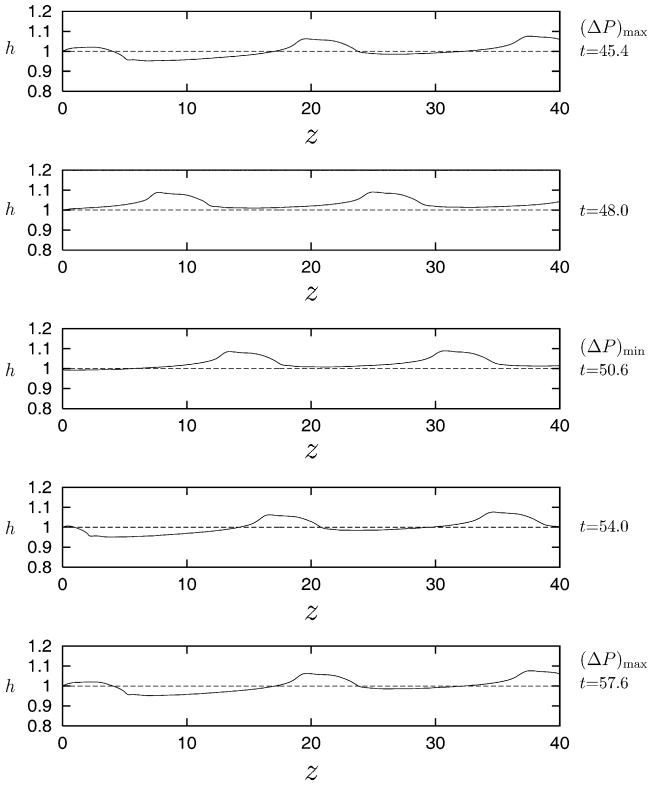

Fig. 21. Free surface oscillations during one cycle: Carreau flow ($n = 0.44$), $Re = 0.01$, $L_b = 20$, and $Q = 1.5$.

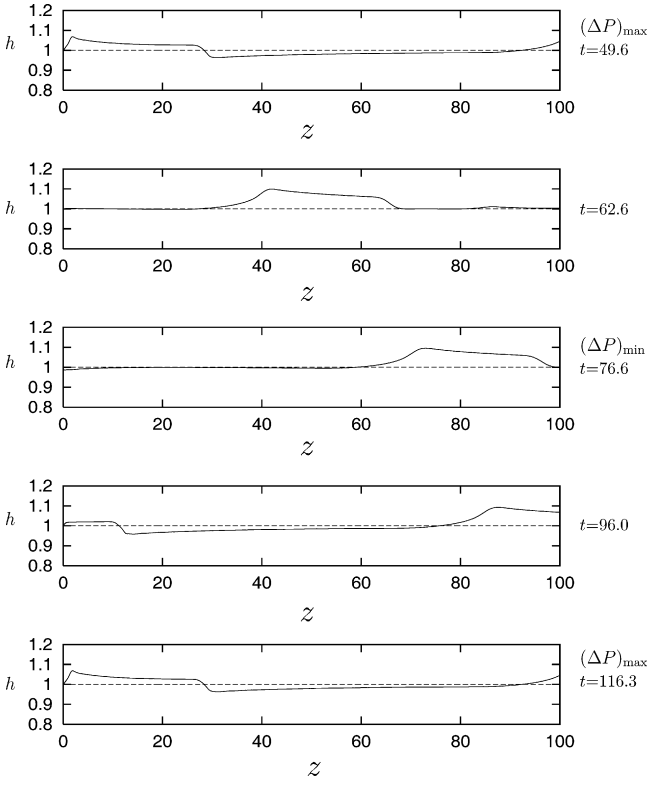

Fig. 22. Free surface oscillations during one cycle: Carreau flow ($n = 0.44$), $Re = 0.01$, $L_b = 80$ and $Q = 1.5$.

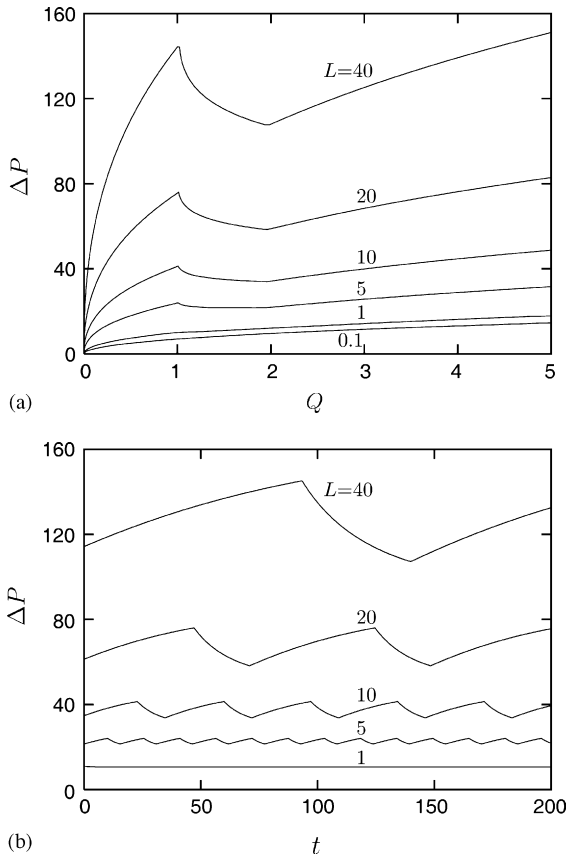

Fig. 23. Flow curves (a) and pressure oscillations (b) for different capillary lengths: Carreau flow ($n = 0.44$), $Re = 0.01$, $Q = 1.35$ and $L_b = 80$.

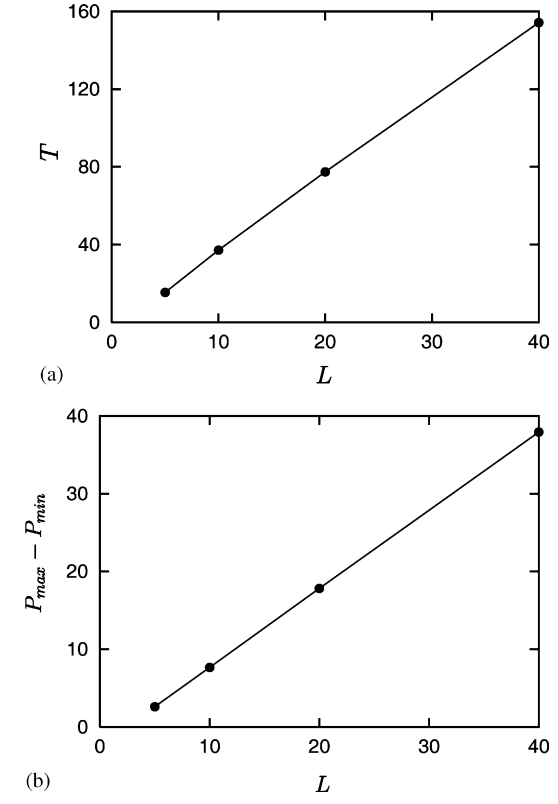

Fig. 24. Period (a) and amplitude (b) of the pressure oscillations as functions of the capillary length: Carreau flow ($n = 0.44$), $Re = 0.01$, $Q = 1.35$ and $L_b = 80$.

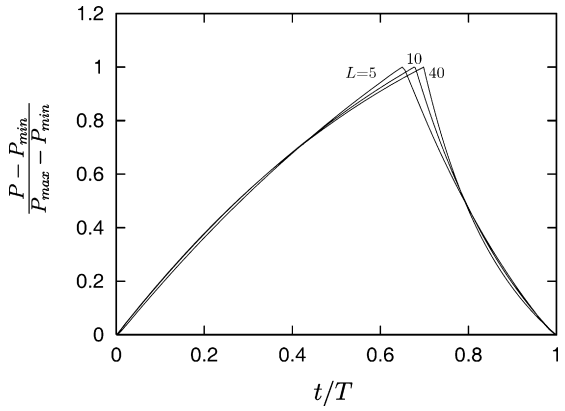

Fig. 25. Normalized pressure oscillations for different capillary lengths: Carreau flow ($n = 0.44$), $Re = 0.01$, $Q = 1.35$ and $L_b = 80$.

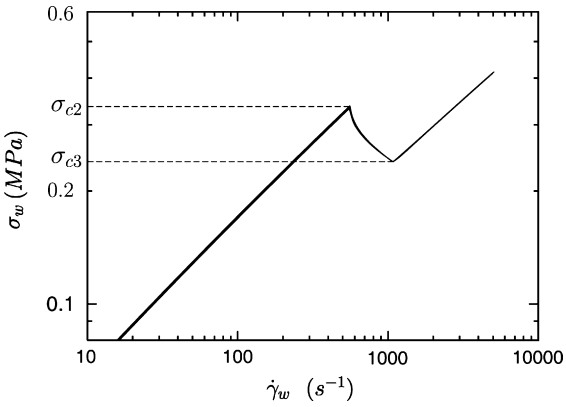

Fig. 26. Apparent wall shear stress vs. the apparent wall shear rate for different capillary lengths: $L = 1$, 5, 10, 20 and 40; Carreau flow ($n = 0.44$) and $Re = 0.01$.

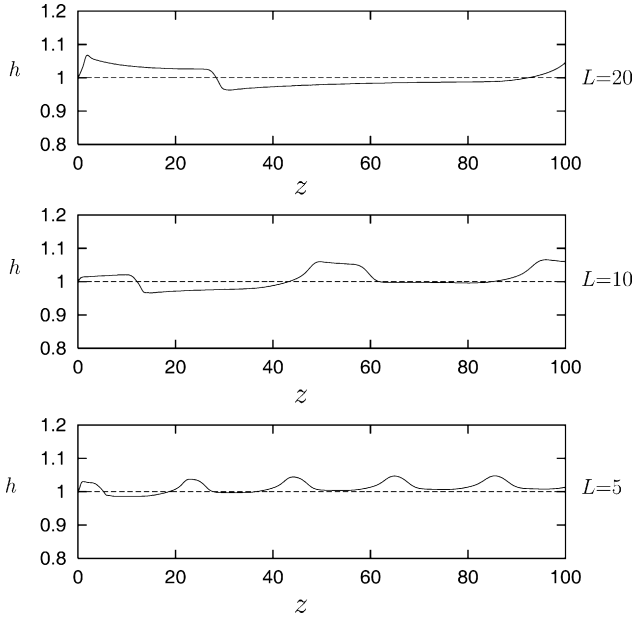

Fig. 27. Free surface oscillations at a pressure drop maximum for different capillary lengths: Carreau flow ($n = 0.44$), $Re = 0.01$ and $L_b = 80$.

4. Conclusions

We used finite elements to simulate the time-dependent, compressible extrusion of a Carreau fluid in the full reservoir-capillary-extrudate geometry, assuming that slip occurs along the die wall following a nonmonotone slip law that is based on the experimental measurements of Hatzikiriakos and Dealy [2,8].

The numerical simulations agree well with the following experimental observations: (a) the pressure and flow rate oscillations follow the hysteresis loop defined by the two branches of the flow curve, and the volumetric flow rate is characterized by instantaneous jumps between the two branches; (b) the amplitude and the period of the pressure oscillations increase linearly with the capillary length, since the hysteresis loop becomes larger; (c) for small capillary lengths, the pressure is a continuous monotonic function of Q, and no oscillations are observed; (d) the period of the pressure and flow rate oscillations increases linearly with the reservoir length, while their amplitudes and waveforms are fairly constant. Nevertheless, the period of the pressure oscillations, when plotted versus the reservoir volume, appears to pass through the origin, which is not the case with extrapolated experimental data [2,3,5,23].

In agreement with certain experiments [17,21,24,27], the period of the pressure oscillations passes through a minimum, when this is plotted versus the imposed volumetric flow rate. The compression part of the pressure oscillations is relatively reduced, as Q is increased.

The calculated value of the critical wall shear stress for the onset of the stick–slip instability, $\sigma_{c2} = 0.34$ MPa, is in the range reported by Hatzikiriakos and Dealy [2]. This value was found to be independent of the capillary length, which is in agreement only with certain experiments [6,29,30]. Unlike experimental observations [2,3], the stick–slip regime is not shifted to lower volumetric flow rates but remains constant as the capillary length is increased. This may be due to the fact that the slip equation we employed does not take into account the pressure dependence of wall slip and holds uniformly across the capillary.

Acknowledgement

This research was partially supported by the Cyprus Foundation for the Promotion of Research (Eureka Programme).

References

[1] G. Georgiou, Stick–slip instability, in: S.G. Hatzikiriakos, K. Migler (Eds.), Chapter 6 in Polymer Processing Instabilities: Control and Understanding, Mercel Dekker Inc., 2004, p. 161.
[2] S.G. Hatzikiriakos, J.M. Dealy, Role of slip and fracture in the oscillating flow of HDPE in a capillary, J. Rheol. 36 (1992) 845.
[3] V. Durand, B. Vergnes, J.F. Agassant, E. Benoit, R.J. Koopmans, Experimental study and modeling of oscillating flow of high density polyethylenes, J. Rheol. 40 (1996) 383.
[4] J.M. Piau, N. El Kissi, Measurement and modelling of friction in polymer melts during macroscopic slip at the wall, J. Non-Newton. Fluid Mech. 54 (1994) 121.
[5] K. Sato, A. Toda, Physical mechanism of stick–slip behavior in polymer melt extrusion: temperature dependence of flow curve, J. Phys. Soc. Jpn. 70 (2001) 3268.

[6] A.V. Ramamurthy, Wall slip in viscous fluids and influence of materials of construction, J. Rheol. 30 (1986) 337.
[7] D.S. Kalika, M.M. Denn, Wall slip and extrudate distortion in linear low-density polyethylene, J. Rheol. 31 (1987) 815.
[8] S.G. Hatzikiriakos, J.M. Dealy, Wall slip of molten high density polyethylenes. II. Capillary rheometer studies, J. Rheol. 36 (1992) 703.
[9] N. El Kissi, J.M. Piau, The different capillary flow regimes of entangled poly-dimethylsiloxane polymers: macroscopic slip at the wall, hysteresis and cork flow, J. Non-Newton. Fluid Mech. 37 (1990) 55.
[10] N. El Kissi, J.M. Piau, Écoulement de fluides polyméres enchêvetrés dans un capillaire. Modélisation du glissement macroscopique á la paroi, CR Acad. Sci. Paris Série II 309 (1989) 7.
[11] K.P. Adewale, A.I. Leonov, Modelling spurt and stress oscillations in flows of molten polymers, Rheol. Acta 36 (1997) 110.
[12] H. Münstedt, M. Schmidt, E. Wassner, Stick and slip phenomena during extrusion of polyethylene melts as investigated by laser-Doppler velocimetry, J. Rheol. 44 (2000) 413.
[13] L. Robert, B. Vergnes, Y. Demay, Flow birefringence study of the stick–slip instability during extrusion of high-density polyethylenes, J. Non-Newton. Fluid Mech. 112 (2003) 27.
[14] M.M. Denn, Extrusion instabilities and wall slip, Annu. Rev. Fluid Mech. 33 (2001) 265.
[15] S.G. Hatzikiriakos, K. Migler (Eds.), Polymer Processing Instabilities: Control and Understanding, Mercel Dekker Inc., New York, 2004.
[16] J.M. Lupton, J.W. Regester, Melt flow of polyethylene at high rates, Polym. Eng. Sci. 5 (1965) 235.
[17] A. Weill, Capillary flow of linear polyethylene melt: sudden increase of flow rate, J. Non-Newton. Fluid Mech. 7 (1980) 303.
[18] G.C. Georgiou, M.J. Crochet, Time-dependent compressible extrudate-swell problem with slip at the wall, J. Rheol. 38 (1994) 1745.
[19] G.C. Georgiou, M.J. Crochet, Compressible viscous flow in slits with slip at the wall, J. Rheol. 38 (1994) 639.
[20] G. Georgiou, The time-dependent compressible Poiseuille and extrudate-swell flows of a Carreau fluid with slip at the wall, J. Non-Newton. Fluid Mech. 109 (2003) 93.
[21] R.W. Myerholtz, Oscillating flow behavior of high-density polyethylene melts, J. Appl. Polym. Sci. 11 (1967) 687.
[22] F.N. Cogswell, Note: on the oscillating flow of HDPE in a capillary, J. Rheol. 37 (1993) 407.
[23] L. Robert, B. Vergnes, Y. Demay, Complex transients in the capillary flow of linear polyethylene, J. Rheol. 44 (2001) 1183.
[24] G.V. Vinogradov, A.Y. Malkin, Y.G. Yanovskii, E.K. Borisenkova, B.V. Yarlykov, G.V. Berezhnaya, Viscoelastic properties and flow of narrow distribution polybutadienes and polyisoprenes, J. Polym. Sci. Part A2 10 (1972) 1061.
[25] C.F.J. Den Doelder, R.J. Koopmans, J. Molenaar, Quantitative modelling of HDPE spurt experiments using wall slip and generalised Newtonian flow, J. Non-Newton. Fluid Mech. 79 (1998) 503.
[26] F.J. Lim, W.R. Schowalter, Wall slip of narrow molecular weight distribution polybutadienes, J. Rheol. 33 (1989) 1359.
[27] S. Okubo, Y. Hori, Model analysis of oscillating flow of high-density polyethylene melt, J. Rheol. 24 (1980) 253.
[28] B. Vergnes, S. d'Halewyn, M.F. Boube, Wall slip and instabilities in the flow of EPDM compounds, in: P. Moldenaers, R. Keunings (Eds.), Theoretical and Applied Rheology, vol. 1, Elsevier, Amsterdam, 1992, p. 399.
[29] S.Q. Wang, P.A. Drda, Superfluid-like stick–slip transition in capillary flow of linear polyethylene. 1. General features, Macromolecules 29 (1996) 2627.
[30] S.Q. Wang, P.A. Drda, Superfluid-like stick–slip transition in capillary flow of linear polyethylene. 2. Molecular weight and low-temperature anomaly, Macromolecules 29 (1996) 4115.
[31] J.L.A. Dubbeldam, J. Molenaar, Dynamics of the spurt instability in polymer extrusion, J. Non-Newton. Fluid Mech. 112 (2003) 217.
[32] J.M. Greenberg, Y. Demay, A simple model of the melt fracture instability, Eur. J. Appl. Math. 5 (1994) 337.
[33] C.F.J. Den Doelder, R.J. Koopmans, J. Molenaar, A.A.F. Van de Ven, Comparing the wall slip and the constitutive approach for modelling spurt instabilities in polymer melt flows, J. Non-Newton. Fluid Mech. 75 (1998) 25.
[34] J. Pérez González, L. Perez-Trejo, L. de Vargas, O. Manero, Inlet instabilities in the capillary flow of polyethylene melts, Rheol. Acta 36 (1997) 677.